

# Inhomogenous Amorphous Content and Enhanced Piezoelectric Properties in $\text{Bi}_{12}\text{TiO}_{20}$ -based Composite Ceramics

**Dan Yu**

Shandong University of Technology

**Minglei Zhao** (✉ [zhaoml@sdu.edu.cn](mailto:zhaoml@sdu.edu.cn))

Shandong University

**Chunlei Wang**

Shandong University

**Jiyuan Fan**

Shandong University of Technology

**Shilei Li**

Shandong University of Technology

**Zhao Li**

Shandong University of Technology

**Yunyan Liu**

Shandong University of Technology

**Cao Wang**

Shandong University of Technology

**Maozeng Lu**

Shandong University of Technology

---

## Rapid Communication

**Keywords:** Piezoelectricity, Flexoelectricity,  $\text{Bi}_{12}\text{TiO}_{20}$ , Composite ceramics

**Posted Date:** January 25th, 2021

**DOI:** <https://doi.org/10.21203/rs.3.rs-152426/v1>

**License:** © ⓘ This work is licensed under a Creative Commons Attribution 4.0 International License.

[Read Full License](#)

---

# Abstract

$\text{Bi}_{12}\text{TiO}_{20}$ -based composite ceramics were prepared by sintering a mixture of presynthesized  $\text{Bi}_{12}\text{TiO}_{20}$  and a second phase around the melting point of  $\text{Bi}_{12}\text{TiO}_{20}$ . These ceramics can exhibit direct as well as inverse piezoelectricity without electrical polarization, and become competitive piezoelectric material with high depoling temperature and stable thermal behavior. However, their piezoelectric constants were, in general, relatively low and do not remain consistent for both the symbol and magnitude over the entire surface. To prevent the permeation of melting  $\text{Bi}_{12}\text{TiO}_{20}$  into substrate and thus create the inhomogeneous amorphous content, samples were sintered on  $\text{Al}_2\text{O}_3$  (0001) single crystal substrate. Compared to samples sintered on  $\text{Al}_2\text{O}_3$  ceramics, piezoelectric coefficient ( $d_{33}$ ) of these samples was increased by 80%. Moreover, the symbol of  $d_{33}$  is identical on the whole surface. Here, the enhanced piezoelectricity might be ascribed to increased alignment of distorted  $\text{BiO}_5$  polyhedra in amorphous  $\text{Bi}_{12}\text{TiO}_{20}$  phase. These results provided a method to improve the piezoelectric properties of  $\text{Bi}_{12}\text{TiO}_{20}$ -based ceramics and provided some inspiration for further development of  $\text{Bi}_{12}\text{TiO}_{20}$ -based ceramics suitable for practical applications.

## 1. Introduction

Traditionally, inorganic piezoelectric materials can be divided into the following two categories: a) ferroelectric single and poly crystals (such as  $\text{BaTiO}_3$ ,  $\text{K}_{0.5}\text{Na}_{0.5}\text{NbO}_3$ ,  $\text{Na}_{0.5}\text{Bi}_{0.5}\text{TiO}_3$  and  $\text{Pb}(\text{Ti}, \text{Zr})\text{O}_3$  piezoelectric ceramics, single crystals, and thin films); b) non ferroelectric but piezoelectric single crystals and oriented thin films (such as  $\text{SiO}_2$ ,  $\text{La}_3\text{Ga}_5\text{SiO}_{14}$  single crystals,  $\text{ZnO}$ ,  $\text{AlN}$  oriented films) [1–5]. Since piezoelectricity cannot exist in central materials, all the above materials are noncentrosymmetric. However, the discovery of flexoelectricity (coupling between strain gradient and poling) extended piezoelectric materials to all insulators [6–8]. According to Lubomirsky et al., some amorphous films (including  $\text{BaTiO}_3$ ,  $\text{BaZrO}_3$  and  $\text{SrTiO}_3$ ) can also show piezoelectricity after passing a temperature gradient [9–12]. These polar amorphous phases are called quasi amorphous phases, and the appearance of polarity is considered as the partial arrangement of local bonding units induced by plastic strain gradient [13]. Yudin and Tagantsev named this effect as plastic flexoelectricity in their review paper, and the design of inorganic materials was then expanded to centrosymmetric amorphous thin films [14].

Recently, we reported a new bulk ceramic that exhibits both positive and inverse piezoelectricity without electric field polarization. These ceramics were prepared by high-temperature interfacial reaction of  $\text{Bi}_{12}\text{TiO}_{20}$  with a second phase such as  $\text{Na}_{0.5}\text{Bi}_{0.5}\text{TiO}_3$ ,  $\text{BaSnO}_3$  and  $\text{BaTiO}_3$  [15–18]. Since  $\text{Bi}_{12}\text{TiO}_{20}$  phase is necessary at present, we call them  $\text{Bi}_{12}\text{TiO}_{20}$ -based ceramics. According to previous studies, there is no obvious oriented grains and the ferroelectric phase is not essential for these polar  $\text{Bi}_{12}\text{TiO}_{20}$ -based ceramics [15, 16]. Inspired by polarization theory of quasi amorphous thin films, this abnormal piezoelectricity may originate from the orientation of distorted  $\text{BiO}_5$  polyhedron of the amorphous  $\text{Bi}_{12}\text{TiO}_{20}$  phase at the grain boundary [17, 18]. Therefore, the polarization effect could also be termed as

plastic flexoelectricity [18].  $\text{Bi}_{12}\text{TiO}_{20}$ -based ceramics have the advantages of low dielectric constant, low dielectric loss, high depoling temperature, and stable thermal behavior. This makes them competitive piezoelectric material for high-temperature applications. However, the polarization mechanism has not been fully elucidated and their piezoelectric constants were, in general, relatively low and do not remain consistent for both the symbol and magnitude over the entire surface. It is an urgent and important task to further verify the origin of this abnormal piezoelectricity and then improve the piezoelectric properties. Previously, the piezoelectric properties were usually improved by changing the main composition or content of the second phase, but with little success [15–18]. This paper presented an effective method to improve the piezoelectricity of  $\text{Bi}_{12}\text{TiO}_{20}$ -based ceramics and discussed the reasons for the improved piezoelectric properties.

## 2. Experimental Section

Here, the starting materials include high purity  $\text{Bi}_2\text{O}_3$ ,  $\text{TiO}_2$  and  $\text{BaCO}_3$  powders. Firstly, barium titanate and  $\text{Bi}_{12}\text{TiO}_{20}$  were synthesized by conventional solid-state reaction route at  $1050^\circ\text{C}$  and  $750^\circ\text{C}$ , respectively. Secondly, barium titanate and  $\text{Bi}_{12}\text{TiO}_{20}$  powders were mixed in the molar ratio of 12:1 and then milled into a disc. Finally, the  $\text{Bi}_{12}\text{TiO}_{20}$ - $\text{BaTiO}_3$  composite was placed on the  $\text{Al}_2\text{O}_3$  (0001) single crystal substrate, and then sintered in  $860^\circ\text{C}$  air atmosphere for about 2 hours. Figure 1 shows the sketch map of the sintering process. According to the thermocouple 1 and thermocouple 2, the temperature difference along thickness direction during sintering process was about  $1 \sim 3^\circ\text{C}$ .

The phase composition was measured by X-ray diffraction meter (XRD) (CuK $\alpha$  Bruker AXS D8 Advance). The surface morphology and distribution of elements were examined by high-resolution scanning electron microscopy (SEM) (HitachiS-4800). The piezoelectric coefficient ( $d_{33}$ ) was tested by YE2730A  $d_{33}$  Meter. The dielectric constants were determined by the LCR analyzer (Agilent 4294A). The element content was analyzed by XPS (Thermo Escalab 250). The local structure and chemical bonding environment were studied by Raman spectroscopy (LaBRAM HR800).

## 3. Results And Discussion

Figures 2(a)-(c) show the XRD patterns of the unsintered composites and the top and bottom surfaces of the sintered sample, respectively. All observed peaks of the unsintered composites belong to  $\text{Bi}_{12}\text{TiO}_{20}$  and  $\text{BaTiO}_3$ , and no impurity phase was found. For the top and bottom surfaces of the sintered sample, the  $\text{Bi}_{12}\text{TiO}_{20}$  and  $\text{BaTiO}_3$  phases were still present. Except for a small (006) diffraction peak of  $\text{Al}_2\text{O}_3$ , no other new crystalline phases were detected. Compared with  $\text{BaTiO}_3$ , the relative intensity of  $\text{Bi}_{12}\text{TiO}_{20}$  on the top and bottom surfaces of the sintered ceramics decreased, indicating that the volume fraction of the  $\text{Bi}_{12}\text{TiO}_{20}$  crystal phase decreased. Since no diffusion halo was found under the diffraction peak, the content of the amorphous phase was limited [19, 20]. There was no significant difference in the relative intensity of  $\text{Bi}_{12}\text{TiO}_{20}$  and  $\text{BaTiO}_3$  phases between the top and bottom surfaces of the sintered sample, so the volume fraction of  $\text{Bi}_{12}\text{TiO}_{20}$  and  $\text{BaTiO}_3$  crystal phases of the top and bottom surfaces had little

difference. For a better comparison, detailed XRD locations of the unsintered composites and sintered sample are given in Fig. 2 (d). After sintering, the XRD peaks of  $\text{Bi}_{12}\text{TiO}_{20}$  and  $\text{BaTiO}_3$  on the top surface of sintered samples obviously moved to a small direction of  $2\theta$ , indicating the slight lattice expansion for crystalline  $\text{Bi}_{12}\text{TiO}_{20}$  and  $\text{BaTiO}_3$  phases [21, 22]. However, the peak shift and lattice expansion were not obvious for the bottom surface. In this case, the lattice expansion may be caused by the residual stress formed during sintering [22].

XRD results showed that sintered sample was mainly composed of crystalline  $\text{BaTiO}_3$ , crystalline  $\text{Bi}_{12}\text{TiO}_{20}$ , and amorphous  $\text{Bi}_{12}\text{TiO}_{20}$ . Figure 3(a) shows a typical SEM image of the sintered sample. It mainly included two distinct forms: small grains which were easy to be identified with grain size of about several hundred nanometers; large size matters that have an irregular shape with the size of about several to a dozen micrometers. According to the EDS spectrum shown in Fig. 3 (b), the small grains corresponded to crystalline  $\text{BaTiO}_3$ , and the large-sized materials corresponded to  $\text{Bi}_{12}\text{TiO}_{20}$  crystal phase with amorphous  $\text{Bi}_{12}\text{TiO}_{20}$  phase distributing on the surface. Because the samples were sintered near the melting temperature of  $\text{Bi}_{12}\text{TiO}_{20}$ , a part of  $\text{Bi}_{12}\text{TiO}_{20}$  was liquid during sintering process. During the cooling process, the fine  $\text{BaTiO}_3$  grains may be wrapped in the irregular  $\text{Bi}_{12}\text{TiO}_{20}$  phase.

The DSC curves of the sintered sample and pure  $\text{Bi}_{12}\text{TiO}_{20}$  ceramic were shown in Fig. 4. For the pure  $\text{Bi}_{12}\text{TiO}_{20}$  ceramic, a strong endothermic peak was present around  $860^\circ\text{C}$ , and the calculated enthalpy ( $\Delta H_1$ ) was  $282.5 \text{ kJ mol}^{-1}$ . This endothermic peak is the melting peak of  $\text{Bi}_{12}\text{TiO}_{20}$  crystalline phase. In comparison, a smaller endothermic peak at approximately  $836^\circ\text{C}$  was present for the sintered sample. The calculated enthalpy ( $\Delta H_2$ ) was approximately  $137.5 \text{ kJ mol}^{-1}$ . This only emerging endothermic peak is also the melting peak of crystalline  $\text{Bi}_{12}\text{TiO}_{20}$ . The melting point of crystalline  $\text{Bi}_{12}\text{TiO}_{20}$  decreased because of the expansion of lattice [23]. Assuming that  $\text{Bi}_{12}\text{TiO}_{20}$  phase in sintered sample was 100% crystalline, the content of crystalline  $\text{Bi}_{12}\text{TiO}_{20}$  phase can be calculated by the ratio of  $\Delta H_2/\Delta H_1$  [24]. According to calculation, about 48% of  $\text{Bi}_{12}\text{TiO}_{20}$  was crystalline. Therefore, we can further estimate an approximately 20% volume fraction of amorphous  $\text{Bi}_{12}\text{TiO}_{20}$  in the sintered sample. Although the sintered sample contained no oriented grains, it can present relatively large piezoelectricity without undergoing an electric poling course. Most of the piezoelectric strain constants ( $d_{33}$ ) were in the range of 13–15pC/N, and the maximum value was increased to 20pC/N. In addition, the symbol of  $d_{33}$  remained almost unchanged over the entire surface. In comparison to  $\text{Bi}_{12}\text{TiO}_{20}$ -based ceramics reported in the past, the piezoelectric constants were greatly improved [18].

Figure 5(a) shows the temperature dependence of dielectric constant and electromechanical coupling coefficient  $k$  (determined by resonance method). The results showed that the dielectric properties of sintered samples were similar to those of pure  $\text{BaTiO}_3$  ceramics [25, 26]. The dielectric curve had a maximum at approximately  $120^\circ\text{C}$ . This temperature corresponded to the Curie temperature of crystalline  $\text{BaTiO}_3$ . There was no macroscopic ferroelectricity in  $\text{BaTiO}_3$  phase, above this temperature [25]. At room temperature, the dielectric constant of the sample was only 280, which was far lower than samples

sintered on Al<sub>2</sub>O<sub>3</sub> ceramics (about 600). It was observed that the  $k$  value had little change between - 50°C and 350°C, and there was no decreasing trend even though the temperature was much higher than the Curie temperature of BaTiO<sub>3</sub>. Therefore, this unusual piezoelectricity appears to have no relationship with crystalline BaTiO<sub>3</sub>. Figure 5(b) shows the piezoelectric resonance frequencies of BaTiO<sub>3</sub> ceramics and the sintered sample as functions of temperature, and the illustration shows the details of piezoelectric resonance frequencies of the sintered sample at 400°C. The experimental results showed that the piezoelectric resonance signal of BaTiO<sub>3</sub> ceramic can be observed at about 180°C. Below this temperature, the tendency of the piezoelectric resonance frequency of the sintered sample was similar to that of BaTiO<sub>3</sub> ceramics. While, above this temperature, the resonance frequency changed slowly with the increase of temperature. The resonance frequency curve can be fitted into a straight line from 250 to 600°C, and the calculated temperature coefficient was about  $100 \times 10^{-6} / ^\circ\text{C}$ . This is an fascinating feature for Bi<sub>12</sub>TiO<sub>20</sub>-based ceramics.

The Bi and Ba elements of the top and bottom surfaces of the sintered sample were quantitatively estimated by XPS. By using C1s signal (284.6eV) as a reference, the high-resolution spectra of the elements determined in the measurement scanning were corrected [27]. The percentages of Bi and Ba elements were calculated by corresponding software. The calculation results showed that the Bi/Ba ratio for the top surface was 1.27, while for the bottom surface was 1.94. Because some small BaTiO<sub>3</sub> grains may be wrapped in Bi<sub>12</sub>TiO<sub>20</sub>, the calculated Bi/Ba ratio may have errors. However, the difference of the Bi/Ba ratio between the top and bottom surfaces indicated that the Bi content of the bottom surface was higher than that of the top surface. The results of XRD showed that the contents of crystalline Bi<sub>12</sub>TiO<sub>20</sub> and BaTiO<sub>3</sub> phase had very little difference. The difference of Bi/Ba ratio according to XPS spectra indicates the different contents of amorphous Bi<sub>12</sub>TiO<sub>20</sub> phase. As shown in Fig. 6, the Ba 3d spectra of the top and bottom surfaces were the same, but for Bi 4f, the peak positions in the bottom surface shifted to the higher binding energies than that obtained in the top surface. The peak shift showed that the content of the amorphous Bi<sub>12</sub>TiO<sub>20</sub> phase in the bottom surface was higher than that in the top surface. This result further proved the inhomogeneity of the content of Bi<sub>12</sub>TiO<sub>20</sub> amorphous phase [12, 27, 28]. Since the amorphous content is limit, the inhomogeneous distribution of amorphous Bi<sub>12</sub>TiO<sub>20</sub> along thickness direction is the main reason for the very low dielectric constant of the sintered sample.

In general, repeated annealing is an effective way of releasing elastic stress [29–31]. The piezoelectric constant of the sintered sample remained unchanged for repeated as well as long time annealing. Figure 7(a) shows detailed XRD comparisons of the unsintered composites and the annealed sample. The XRD peak position of annealed sample was similar to that of unsintered composites, which confirmed the release of the elastic residual stress. Thus, the elastic deformation of crystalline phase should not be the main contributor of this abnormal piezoelectricity. Figure 7(b) shows the Raman spectra of Bi<sub>12</sub>TiO<sub>20</sub> standard sample and the annealed sample. The Raman peaks of the annealed sample can be divided into two groups: p1-p10 which is related to Bi<sub>12</sub>TiO<sub>20</sub> [31, 32] and p11-p13 which is related to BaTiO<sub>3</sub>[33] (Bi<sub>12</sub>TiO<sub>20</sub> and BaTiO<sub>3</sub> peaks completely overlapped at approximately  $720\text{cm}^{-1}$ ).

The vibration modes of  $\text{Bi}_{12}\text{TiO}_{20}$  include the  $\text{TiO}_4$  tetrahedron mode which appeared above  $700\text{cm}^{-1}$  and the  $\text{BiO}_5$  polyhedron mode at low frequency. In order to study the detailed contrast of Raman spectra, an extended view near p1, p2, p10/p13 peaks is shown in the illustration. Compared with the Raman peak of  $\text{Bi}_{12}\text{TiO}_{20}$  standard sample, p10/p13 peak had no obvious change. This suggests that the  $\text{TiO}_4$  tetrahedra remained unchanged. However, the p1 and p2 peaks in the top and bottom surfaces of the annealed sample moved almost the same degree towards lower wavenumber direction. As a reflection of Bi-O bond vibrations of  $\text{BiO}_5$  polyhedra, the movement of these peaks indicates the asymmetric elongation of the Bi-O bond and further confirms the expanded distortion of the  $\text{BiO}_5$  polyhedra. Combining with the XRD spectra, the expansion was related with amorphous structure. By comparing the Raman spectra near the top and bottom surfaces, the  $\text{BiO}_5$  polyhedra distorted at approximately the same degree. The uniform deformation degree of  $\text{BiO}_5$  polyhedra along thickness direction may result in the enhancement of piezoelectric constant.

The difference of the preparation process between the sintered sample and the previously reported  $\text{Bi}_{12}\text{TiO}_{20}$ -based ceramics is only the substrate used during sintering process. Since all  $\text{Bi}_{12}\text{TiO}_{20}$ -based ceramics were sintered near the melting point of  $\text{Bi}_{12}\text{TiO}_{20}$ ,  $\text{Bi}_{12}\text{TiO}_{20}$  phase was partially liquid. The liquid  $\text{Bi}_{12}\text{TiO}_{20}$  phase tended to move downward under the action of gravity. The movement of liquid  $\text{Bi}_{12}\text{TiO}_{20}$  resulted in a small composition gradient and a certain orientation along the thickness direction. During natural cooling process, the crystalline  $\text{BaTiO}_3$  phase and  $\text{Al}_2\text{O}_3$  single crystal substrate could inhibit the recrystallization of  $\text{Bi}_{12}\text{TiO}_{20}$ , thus result in the forming and maintaining of the gradient of  $\text{Bi}_{12}\text{TiO}_{20}$  amorphous content and the orientation of distorted  $\text{BiO}_5$  polyhedra. Since the temperature gradient is rather small, the alignment of distorted  $\text{BiO}_5$  polyhedron might be lead by the movement of  $\text{Bi}_{12}\text{TiO}_{20}$  liquid phase [34]. As the substrate was  $\text{Al}_2\text{O}_3$  ceramics that had defects, the liquid  $\text{Bi}_{12}\text{TiO}_{20}$  phase will gradually fill the apparent pores of the substrate, thus the composition gradient was greatly reduced.

## 4. Conclusions

In conclusion, the  $\text{Al}_2\text{O}_3$  single crystal substrate sintering method is an effective way to enhance the piezoelectric properties of the  $\text{Bi}_{12}\text{TiO}_{20}$ -based ceramics. In this study, the piezoelectric strain constant was increased to  $20\text{pC/N}$ . In addition, the prepared sample has high mechanical coupling coefficient, high depoling temperature and temperature stability of resonance frequency in a certain temperature range, which is an ideal material for high temperature piezoelectric materials. These results provided a method to improve the piezoelectric properties of  $\text{Bi}_{12}\text{TiO}_{20}$ -based ceramics, and provided inspiration for further research on developing  $\text{Bi}_{12}\text{TiO}_{20}$ -based ceramics suitable for practical applications.

## Declarations

## Acknowledgements

This work was supported by the National Nature Science Foundation of China (No. 51172129), and the Natural Science Foundation of Shandong (Nos.ZR2020QA058, ZR2017MEM008, ZR2019MA036, ZR2020QE215 and ZR2020QA070).

## References

1. Fritze, H., and Tuller, H. L. Langasite for high-temperature bulk acoustic wave applications, *Appl. Phys. Lett.* 2001, **78**: 976-977.
2. Haines, J. , Cambon, O. , Prudhomme, N. , Fraysse, G. , Keen, D. A. , & Chapon, L. C. , et al. High-temperature, structural disorder, phase transitions and piezoelectric properties of  $\text{GaPO}_4$ , *Phys. Rev. B* 2006, **73**: 014103.
3. S. J. Zhang, Y. T. Fei, B. H. T. Chai, E. Frantz, D. W. Snyder, X. N. Jiang, and T. R. Shroud, Characterization of piezoelectric single crystal  $\text{YCa}_4\text{O}(\text{BO}_3)_3$  for high temperature applications, *Appl. Phys. Lett.* 2008, **92**: 202905.
4. R. C. Turner, P. A. Fuierer, R. E. Newnham, and T. R. Shroud, Materials for high temperature acoustic and vibration sensors: A review, *Appl. Acoust.* 1994, **41**: 299-324.
5. M. J. Davis, P. Vullo, I. Mitra, P. Blaum, K. A. Gudgel, N. J. Donnelly, and C. A. Randall, Ferroelectric and Nonferroelectric (Polar) Piezoelectric Glass-Ceramics, *J. Am. Ceram. Soc.* 2008, **1**: 2878-2885.
6. K. A. Tagantsev, Piezoelectricity and flexoelectricity in crystalline dielectrics, *Phy. Rev. B* 1986, **34**: 5883.
7. J. Fousek, L. E. Cross, D. B. Litvin, Possible piezoelectric composites based on the flexoelectric effects, *Mater. Lett.* 1999, **39** : 287-291.
8. Sharma, N. D. , R. Maranganti, and P. Sharma, On the possibility of piezoelectric nanocomposites without using piezoelectric materials, *J. Mech. Phys. of Solids* 2007, **55**: 2328-2350.
9. V. Lyahovitskaya, I. Zon, Y. Feldman, S.R. Cohen, A.K. Tagantsev, I. Lubomirsky, Pyroelectricity in highly stressed quasi-amorphous thin films, *Adv. Mater.* 2003, **15**: 1826-1828.
10. V. Lyahovitskaya, Y. Feldman, I. Zon, E. Wachtel, K. Gartsman, A.K. Tagantsev, I. Lubomirsky, Formation and thermal stability of quasi-amorphous thin film, *Phys. Rev. B* 2005, **71**: 94205.
11. A. I. Frenkel, Y. Feldman, V. Lyahovitskaya, E. Wachtel, I. Lubomirsky, Microscopic origin of polarity in quasicrystalline  $\text{BaTiO}_3$ , *Phys. Rev. B* 2005, **71**: 024116.
12. D. Ehre, V. Lyahovitskaya, A. Tagantsev, I. Lubomirsky, Amorphous piezo- and pyroelectric phases of  $\text{BaZrO}_3$  and  $\text{SrTiO}_3$ , *Adv. Mater.* 2007, **19**: 1515-1517.
13. E. Wachtel, I. Lubomirsky, Quasi-amorphous inorganic thin films: non-crystalline polar phases, *Adv. Mater.* 2010, **22**: 2485-2493.
14. P. V. Yudin, A. K. Tagantsev, Fundamentals of flexoelectricity in solids, *Nanotechnology* 2013, **24**: 423001.

15. M. L. Zhao, L. H. Wang, C. L. Wang, J. L. Zhang, Z. G. Gai, C. M. Wang, J. C. Li, Interface-induced piezoelectricity in an unpoled  $\text{Na}_{0.5}\text{Bi}_{0.5}\text{TiO}_3$ -based composite ceramic, *Appl. Phys. Lett.* 2009, **95**.
16. D. Yu, M. L. Zhao, C.L. Wang, L.H. Wang, J. Wang, Z.G. Gai, J.L. Zhang, Piezoelectricity in non-ferroelectric  $\text{Bi}_{12}\text{TiO}_{20}$ - $\text{BaSnO}_3$  amorphous ceramics, *Phys. Status Solidi B* 2015 **252** (10) () 2174-2178.
17. D. Yu, M. L. Zhao, C. L. Wang, L. H. Wang, Z. G. Gai, C. M. Wang, J. L. Zhang, J. C. Li, Amorphous phases and composition dependence of piezoelectricity in  $\text{BaTiO}_3$ - $\text{Bi}_2\text{O}_3$  polar amorphous ceramics, *Ceram. Int.* 2016, **42**: 1777-1781.
18. D. Yu, M. L. Zhao, C. L. Wang, L. H. Wang, W. B. Su, Z. G. Gai, C. M. Wang, J. C. Li, J. L. Zhang, Enhanced piezoelectricity in plastically deformed nearly amorphous  $\text{Bi}_{12}\text{TiO}_{20}$ - $\text{BaTiO}_3$  nanocomposites, *Appl. Phys. Lett.* 2016, **109**: 1083.
19. Tiainen, Minna , J. Daavitsainen , and R. S. Laitinen, The role of amorphous material in ash on the agglomeration problems in FB boilers: A powder XRD and SEM-EDS study, *Energy & Fuels* 2002, **16**: 871-877.
20. Ouhadi, V. R., and R. N. Yong, Impact of clay microstructure and mass absorption coefficient on the quantitative mineral identification by XRD analysis, *App. Clay. Sci.* 2003, **23**: 141-148.
21. Tadahiko, Furuta, Shigeru, Kuramoto, Junghwan, Hwang, Elastic deformation behavior of multi-functional Ti-Nb-Ta-Zr-O alloys, *Mater. Tran.* 2005, **46**: 3001-3007.
22. Rickerby, D. S., Eckold, G., Scott, K. T., Buckley-Golder, The interrelationship between internal stress, processing parameters and microstructure of physically vapour deposited and thermally sprayed coatings, *Thin Solid Films* 1987, **154**: 125-141.
23. Suresh, Arun, et al. Crystallite and Grain-Size-Dependent Phase Transformations in Yttria-Doped Zirconia, *J. Am. Ceram. Soc.* 2003, **86**.
24. Zhu, Yan, C. Lishan, and Z. Yanjun, Effects of plate thickness on reverse martensitic transformation of prestrained NiTi/NiTi alloy, *Fron. of Mater. China* 2007, **1**: 356-358.
25. K. Kinoshita, A. Yamaji, Grain-size effects on dielectric properties in barium titanate ceramics, *J. Appl. Phys* 1976, **47**: 371-373.
26. Mccauley, Daniel, R. E. Newnham, and C. A. Randall, Intrinsic Size Effects in a Barium Titanate Glass-Ceramic, *J. Am. Ceram. Soc.* 1998, **81**: 979-987.
27. Kumar, S., Raju, V. S., Bera, S., Vijaynandhini, K., Kutty, T. R. N., Studies on surface composition and chemical states of calcium manganites, *Appl. Surf. Sci.* 2005, **237**: 623-630.
28. Ehre D., Cohen H., Lyahovitskaya V., and Lubomirsky I, X-ray photoelectron spectroscopy of amorphous and quasiamorphous phases of  $\text{BaTiO}_3$  and  $\text{SrTiO}_3$ , *Phys. Rev. B* 2008, **77**: 998-1002.
29. B. G. Cohen and M. W. Focht, X-ray measurement of elastic strain and annealing in semiconductors, *Solid-St. Electron* 1970. **9**: 461.
30. Ozkan, C. S., W. D. Nix, and H. Gao, Strain relaxation and defect formation in heteroepitaxial  $\text{Si}_{1-x}\text{Ge}_x$  films via surface roughening induced by controlled annealing experiments, *Appl. Phys. Lett.* 1997, **70**:

2247-2249.

31. Pezzotti, Giuseppe, A. Nakahira, and M. Tajika, Effect of extended annealing cycles on the thermal conductivity of AlN/Y<sub>2</sub>O<sub>3</sub> ceramics, J. Eur. Cera. Soc.2000, **20**: 1319-1325.
32. L. Wiehl, A. Friedrich, E. Haussühl, W. Morgenroth, A. Grzechnik, K. Friese, B. Winkler, K. Refson, V. Milman, Structural compression and vibrational properties of Bi<sub>12</sub>SiO<sub>20</sub> sillenite from experiment and theory, J. Phys.: Condens. Matter 2010, **22**: 505401.
33. W.H. Zhang, L. Chen, Y.T. Tao, W.H. Zhang, J. Chen, J.X. Zhang, Raman study of barium titanate with oxygen vacancies, Phys. B 2011, **406**: 4630-4633.
34. J. Karthik, R. V. K. Mangalam, J. C. Agar, and L. W. Martin, Large built-in electric fields due to flexoelectricity in compositionally graded ferroelectric thin films, Phys. Rev. B 2013, **87**: 024111.

## Figures

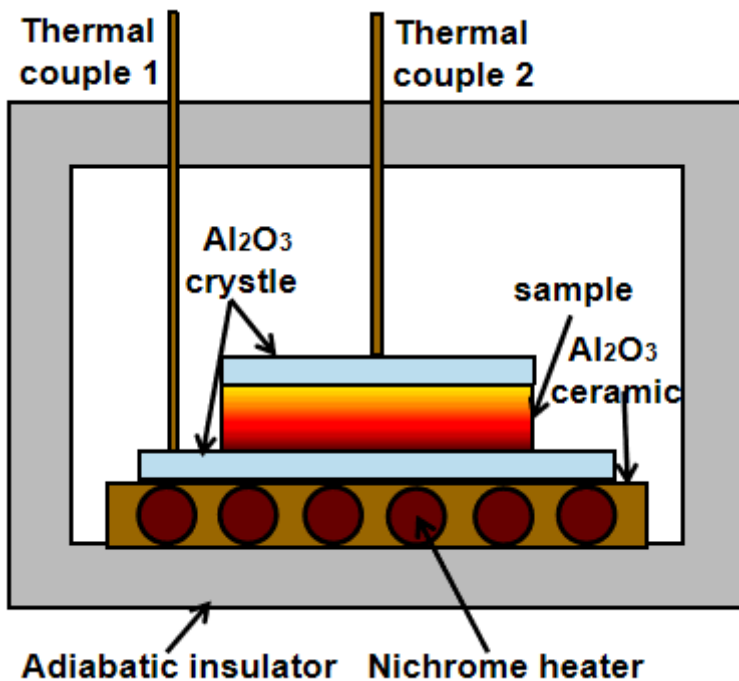


Figure 1

The schematic illustration of the sintering process.

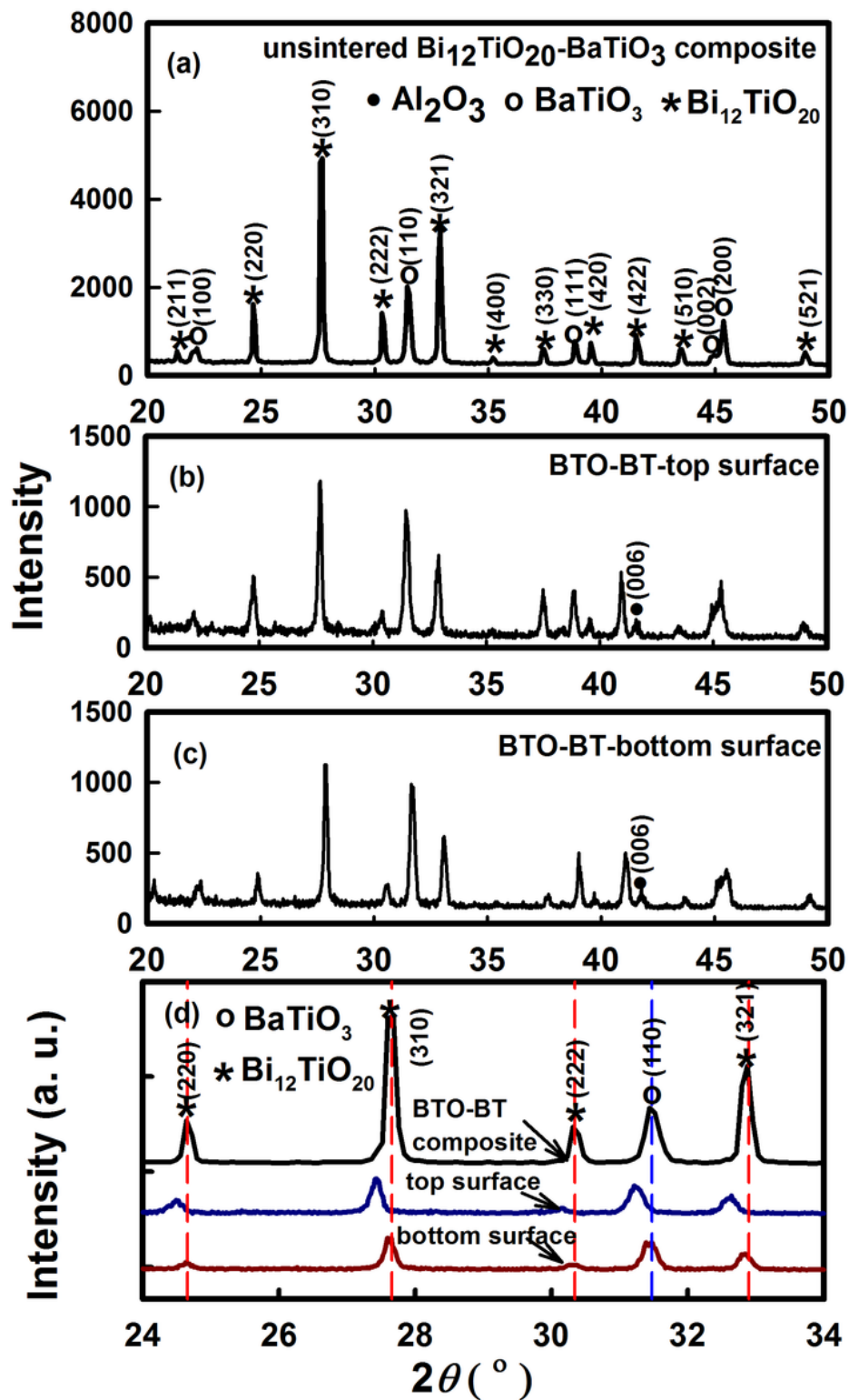
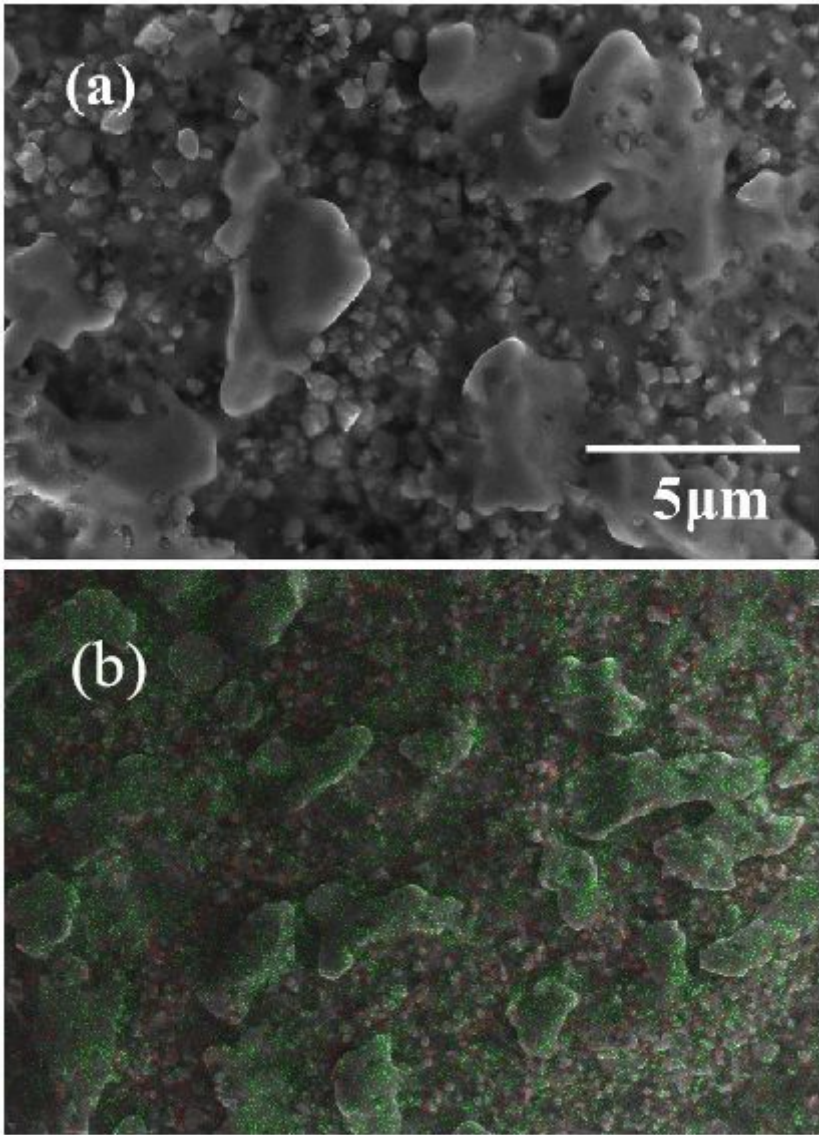


Figure 2

The XRD patterns of (a) the unsintered composites; (b) the top surface of sintered sample; (c) the bottom surface of the sintered sample; (c) the unsintered composites and sintered sample.



**Figure 3**

(a) SEM image; (b) EDS mapping of Bi (green) and Ba (red) for cross-section of the sintered sample.

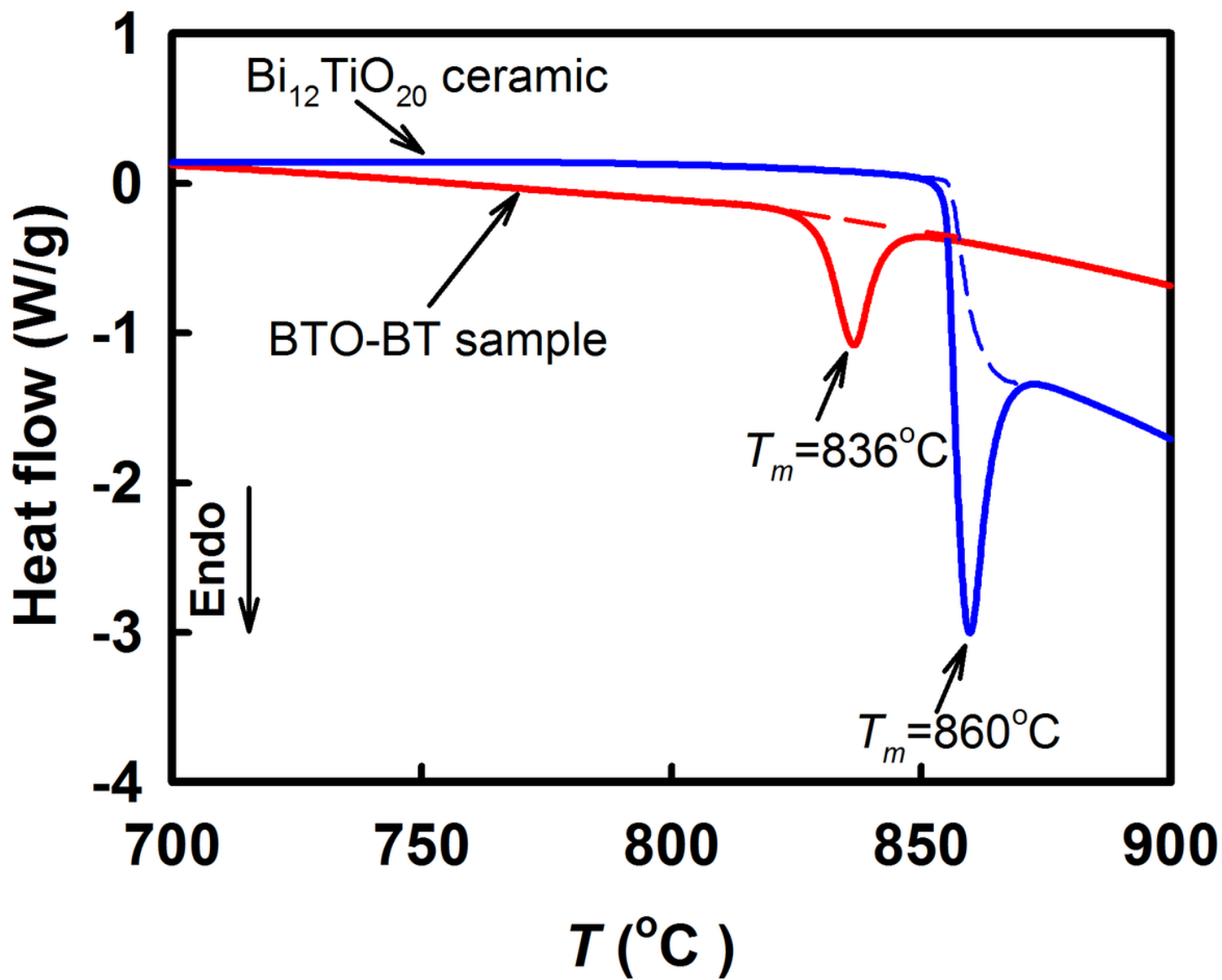


Figure 4

DSC curves of the sintered sample and the Bi<sub>12</sub>TiO<sub>20</sub> ceramic.

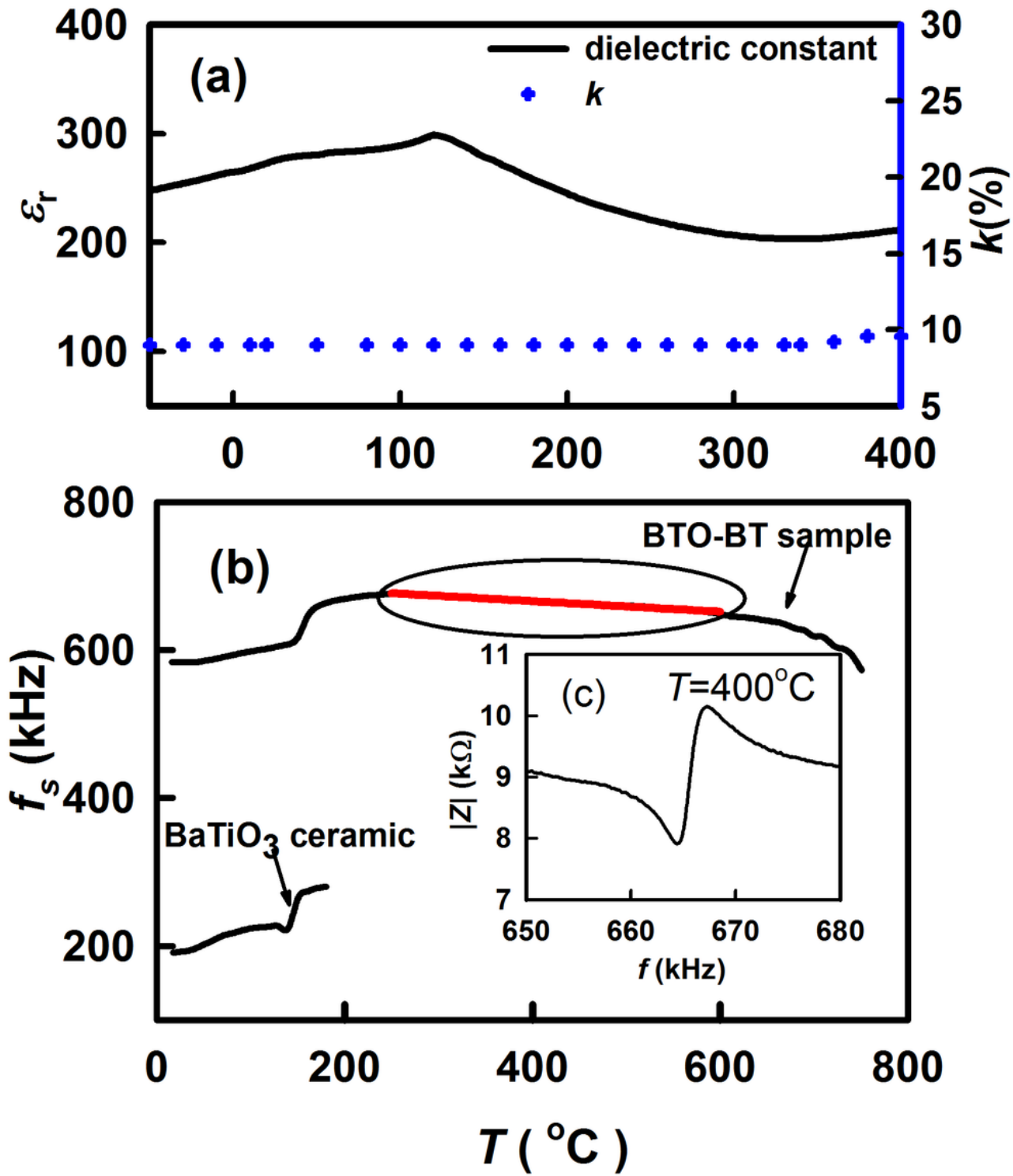


Figure 5

(a) dielectric constant and electromechanical coupling factor; (b) resonance frequency of sintered sample and BaTiO<sub>3</sub> ceramic as a function of temperature.

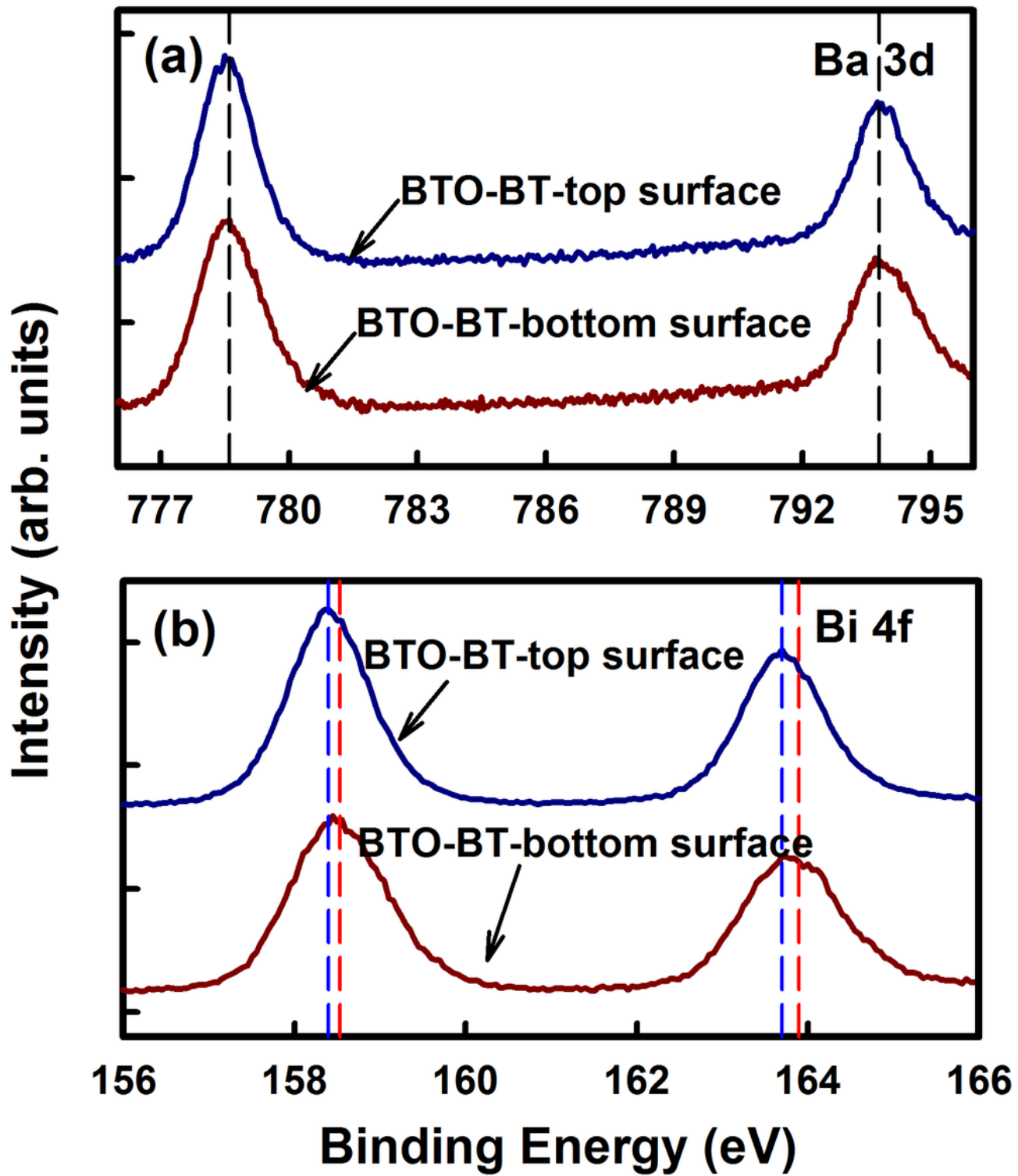


Figure 6

(a) Ba 3d; (b) Bi 4f XPS spectra of the sintered sample.

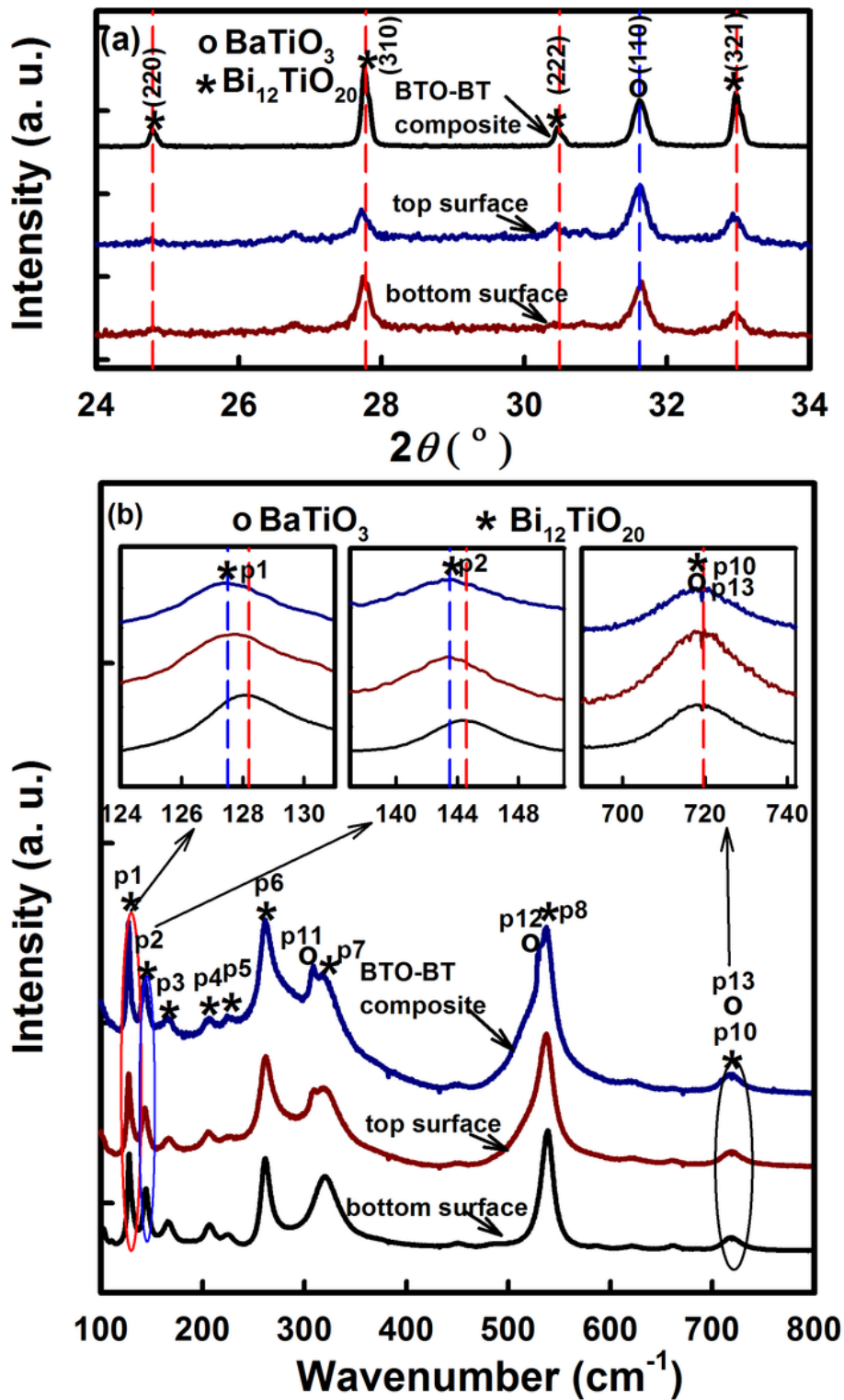


Figure 7

(a) The XRD patterns of the composites and annealed sample; (b) The spectra of the anneal sample and  $\text{Bi}_{12}\text{TiO}_{20}$  ceramic.